machines

MDPI

Article

C3bot: A Climbing Robot for 3D Variable-Curvature Structures †

Mingyuan Wang [1,2], Yize Xu [1,2], Ziqing Gu [1,2], Jianjun Yuan [1,2,*], Sheng Bao [1,2] and Zhengtao Hu [1,2,*]

[1] School of Mechatronic Engineering and Automation, Shanghai University, Shanghai 200444, China
[2] Shanghai Key Laboratory of Intelligent Manufacturing and Robotics, Shanghai University, Shanghai 200444, China
* Correspondence: terabit@shu.edu.cn (J.Y.); huzhengtao14z@gmail.com (Z.H.)
† This paper is an extended version of our published paper: Xu, K.; Hu, M.; Deng, Z.; Wang, M.; Yuan, J.; Xu, Y. Design and Validation of a Climbing Robot via Passive Wheel Compliance. In Proceedings of the IEEE International Conference on Cyborg and Bionic Systems 2025, Beijing, China.

Abstract

To improve the adaptability and adhesion of wall-climbing robots on complex curved surfaces, a self-adaptive spherical magnetic wheel robot is proposed for inspecting three-dimensional variable-curvature structures. The robot employs a bilateral wheeled design with passive magnetic modules that automatically adjust to contact conditions, ensuring efficient adhesion without active control. A Halbach-array magnetic circuit further enhances adhesion without increasing size or weight. Simulations analyze the effect of swing angle on adhesion and determine the minimum adaptable curvature radius. Experiments show stable climbing on surfaces with radii of 100–350 mm, obstacle-crossing up to 7 mm, and a payload capacity of 16.63 kg. Compared with existing designs, the robot offers improved curvature adaptability and load capacity under similar size and weight constraints.

Keywords: climbing robot; curvature adaptation; magnetic adhesion; mechanical design

1. Introduction

In the fields of energy, chemical industry, and large-scale equipment manufacturing, critical components such as transmission pipelines [1,2], turbine blades [3,4], storage tank outer walls, and ship hull structures [5,6] commonly exhibit complex three-dimensional curved surfaces. During long-term operation, these structures are prone to problems such as corrosion, cracks, material fatigue, and coating degradation. If not detected and maintained in a timely manner, these defects may lead to serious safety accidents. Therefore, periodic inspection and condition assessment of their external surfaces play a vital role in maintaining the safe and reliable operation of these systems.

At present, the maintenance of these structures still mainly relies on manual operations using scaffolding or lifting equipment. This approach not only poses significant safety risks but also involves high labor intensity and low efficiency. Meanwhile, inspection results are easily influenced by the experience of operators, making it difficult to guarantee sufficient inspection coverage and accuracy. In addition, equipment downtime is often directly related to the duration of manual maintenance, which further increases operational costs. Therefore, replacing manual maintenance operations with automated equipment has become an inevitable trend [7,8].

Wall-climbing robots can adhere to working surfaces and carry onboard equipment to perform tasks such as locomotion and inspection, making them a promising alternative to manual operations. Based on their adhesion principles, wall-climbing robots are generally

Check for updates

Received: 10 March 2026
Revised: 11 April 2026
Accepted: 21 April 2026
Published: 28 April 2026

Copyright: © 2026 by the authors. Licensee MDPI, Basel, Switzerland. This article is an open access article distributed under the terms and conditions of the Creative Commons Attribution (CC BY) license.

divided into three main categories: vacuum adhesion robots [9,10], bio-inspired adhesion robots [11,12], and magnetic adhesion robots [13,14]. Vacuum adhesion provides a large load capacity; however, it is difficult to maintain reliable sealing under specific surface curvatures and structural configurations, and its mobility is relatively limited. Bio-inspired adhesion exhibits good performance on specific material surfaces, but its load capacity is relatively low and the control is usually complex. For metallic structures, magnetic adhesion offers advantages such as compact structure, stable adhesion force, and relatively simple control, making it more suitable for operations on complex surfaces [15,16].

Most existing adhesion-based wall-climbing robots adopt rigid chassis structures, in which the relative positions between adhesion and locomotion units are fixed [6,17]. When operating on three-dimensional surfaces with significant curvature variations, large gaps may arise between the robot and the contact surface, leading to serious failure modes such as detachment and jamming, thereby limiting their adaptability to complex geometries [18,19].

To address this issue, various strategies have been proposed to regulate the relative posture between adhesion modules and locomotion units to better match surface curvature and reduce contact gaps. One approach is to introduce actively controllable degrees of freedom in the adhesion modules, allowing adjustment of the magnitude and direction of the adhesion force [20–22]. This method is structurally compact and flexible; however, its performance highly depends on control accuracy, leading to increased operational complexity. In addition, the use of multiple actuators increases system size and weight, thereby reducing mobility and payload capacity. Another approach involves the use of passive or semi-active suspension mechanisms to adjust the inclination of adhesion and locomotion units, enabling better conformity to curved surfaces [23–26]. These systems typically require only a limited number of actuators and offer a certain degree of self-adaptability without complex control. However, the introduction of additional suspension structures significantly increases the chassis size, which may lead to collisions or jamming when operating on surfaces with small curvature radii or abrupt geometric variations. A third approach is inspired by biological locomotion, where novel adhesion and locomotion mechanisms are designed based on bio-inspired principles [27]. These robots are generally more flexible and compact, and can achieve high adhesion efficiency. Nevertheless, they often suffer from limited payload capacity and reduced motion stability, restricting their applicability to practical inspection and maintenance tasks. In addition, recent studies have investigated robotic operational reliability and constrained motion control under uncertainties [28,29]. By combining kinematic and dynamic modeling with adaptive control strategies incorporating disturbance observers, the motion reliability and robustness of the system are improved.

Although existing wall-climbing robots can adapt to surfaces with varying curvatures, they are generally limited to large-curvature or convex surfaces. In addition, some designs require multiple actuators, resulting in high system complexity, as summarized in Table 1. To address these limitations, a wheeled wall-climbing robot for inspection tasks, named C3bot (Climbing 3D Robot), is proposed. Compared with existing wall-climbing robots, the main contributions of this work are as follows: (1) A two-degree-of-freedom passive magnet holder is adopted to automatically adjust the adhesion direction, improving adaptability to three-dimensional curved surfaces without complex control. (2) A spherical wheel configuration enables more compact contact with the surface, allowing the robot to operate on more extreme curved geometries. (3) A Halbach-array-based magnetic circuit is designed to enhance adhesion performance without increasing the system size, thereby improving stability on variable-curvature surfaces.

Table 1. Survey of prior wall-climbing robots and our design.

Robot	Size	Mobile Type	Minimum Adaptable Radius of Curvature (Convex/Concave)	Adhesion Method	Number of Motors	Functions of the Robot
Yang et al. [20]	510 × 534 × 180 mm	2 Crawlers	2500 mm/2500 mm	Magnetic (Untouched)	2	Maintenance and inspection
Cui et al. [21]	Unmentioned	Wheel-legged	Unmentioned	Magnetic	6	Vision inspection
Eto and Asada. [22]	307 × 480 × 185 mm	4 Wheels	200 mm/200 mm	Magnetic	8	Welding
Hu et al. [23]	1400 × 1010 × 400 mm	2 Crawlers	3000 mm/Unable	Magnet	2	Maintenance and inspection
Tavakoli et al. [24]	246 × 246 × 90 mm	3 Wheels	300 mm/300 mm	Magnetic	3	Inspection
Jiang et al. [25]	680 × 413 × 204 mm	4 Wheels	1200 mm/Unable	Magnetic	2	Maintenance and inspection
Wang et al. [26]	625 × 573 × 303 mm	2 Crawlers	1000 mm/1000 mm	Magnetic (Untouched)	2	Maintenance and inspection
Khan et al. [27]	40 × 40 × 560 mm	2 Legs	Unmentioned	Magnetic	5	/
C3bot (This paper)	312 × 210 × 176 mm	4 Wheels	188 mm/120 mm	Magnetic (Untouched)	2	Vision inspection, ultrasonic detection

This paper is an extended version of our previous conference paper [30]. Compared with the conference version, this work provides a more detailed and systematic design of the robot's mechanical structure and a deeper analysis of the magnetic adhesion mechanism, establishing the relationship between the swing angle and adhesion force. In addition, the kinematic behavior of the robot on curved surfaces is investigated, particularly considering the integration of inspection actuators (e.g., ultrasonic probes). Furthermore, the experimental validation is expanded, including adhesion force tests, climbing tests on surfaces with different curvatures, safety rope tension tests, obstacle-crossing experiments, and validation in a practical turbine blade inspection scenario.

The remainder of this paper is organized as follows: Section 2 introduces the mechanical structure and working principle of the robot. Section 3 analyzes the static state of the robot and calculates the minimum magnetic attraction force required for a single magnetic spherical wheel. Section 4 presents a parametric simulation analysis of the magnetic spherical wheel. Section 5 analyzes the robot's motion and derives its surface adaptability. Section 6 presents the prototype development and experimental validation under various conditions. Section 7 concludes the paper.

2. Mechanical Structure of the Wall-Climbing Robot

2.1. Concept Design of the Magnetic Spherical Wheel

From a manufacturing and cost perspective, most robots use traditional cylindrical permanent magnetic wheels. When contacting variable-curvature surfaces, these wheels can cause magnetic force feedback torque issues on the robot body due to non-fixed contact points, as illustrated in Figure 1a. If a spherical wheel with a smaller radius of curvature than the adhesion surface is used for contact, no additional torque will be generated. Meanwhile, the adhesion direction also needs to adapt to changes in contact

points. Therefore, this paper proposes the design of a magnetic spherical wheel, as shown in Figure 1b. The normal force from the curved surface passes through the contact point and is perpendicular to the common tangent at that point, thereby avoiding the generation of additional torque. This improves the robot's force characteristics and enhances its adaptability to curved surfaces.

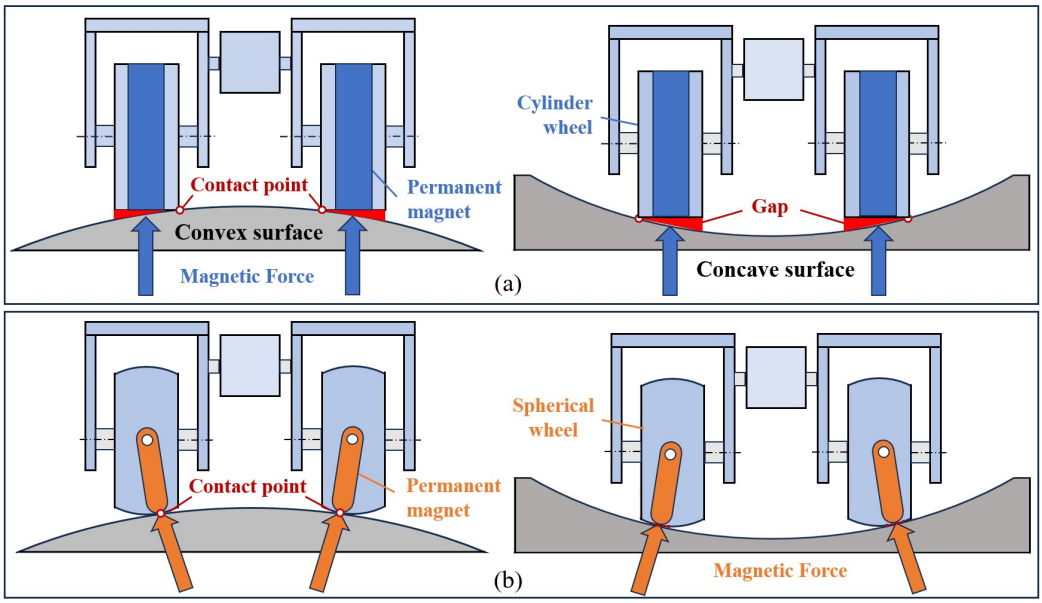


Figure 1. Robot adaptive principle: (**a**) traditional magnetic wheel; (**b**) magnetic spherical wheel.

2.2. Mechanical Design of the Robot

Figure 2a presents the overall view of C3bot, whose dimensions are 320 mm × 230 mm × 180 mm. The two mechanical cantilevers of the robot (Figure 2b) are connected through a differential center (Figure 2c). During locomotion on a three-dimensional curved structure, the two mechanical cantilevers can rotate relative to each other to eliminate the individual variations in the gap between each wheel and its corresponding contact surface. This mechanism enables the robot and its onboard inspection devices, such as ultrasonic probes, to remain in contact with the curved surface, thereby ensuring the continuity and reliability of the robot motion. Two magnetic spherical wheels (Figure 2d) are mounted on each mechanical cantilever. Inside each spherical wheel, a magnet holder with two passive rotational degrees of freedom is integrated (Figure 2e). One rotation occurs along the wheel axis, and the other is perpendicular to it, guaranteeing that the magnetic adhesion force always acts normal to the surface and providing dependable adaptation to surfaces with varying curvature.

Figure 3 illustrates the posture of the magnet holder when the robot contacts different types of surfaces. When the robot is in contact with a flat surface, the magnet holder does not swing. When the robot contacts convex and concave surfaces, the magnet holder swings inward and outward, respectively. Since the posture of the magnet holder automatically adjusts according to the contact condition, the robot can maintain maximum adhesion efficiency by only regulating its moving speed, without requiring additional complex control, thereby enabling reliable motion on complex three-dimensional curved surfaces.

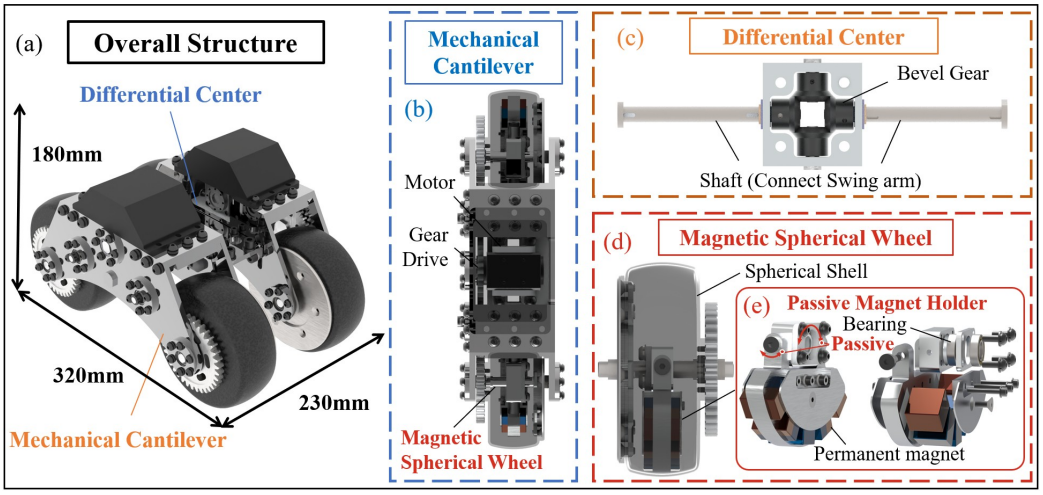


Figure 2. Overall structure of the C3bot: (**a**) Robot appearance and dimensions. (**b**) Mechanical cantilevers. (**c**) Differential center. (**d**) Magnetic spherical wheel. (**e**) Passive adaptive magnet support.

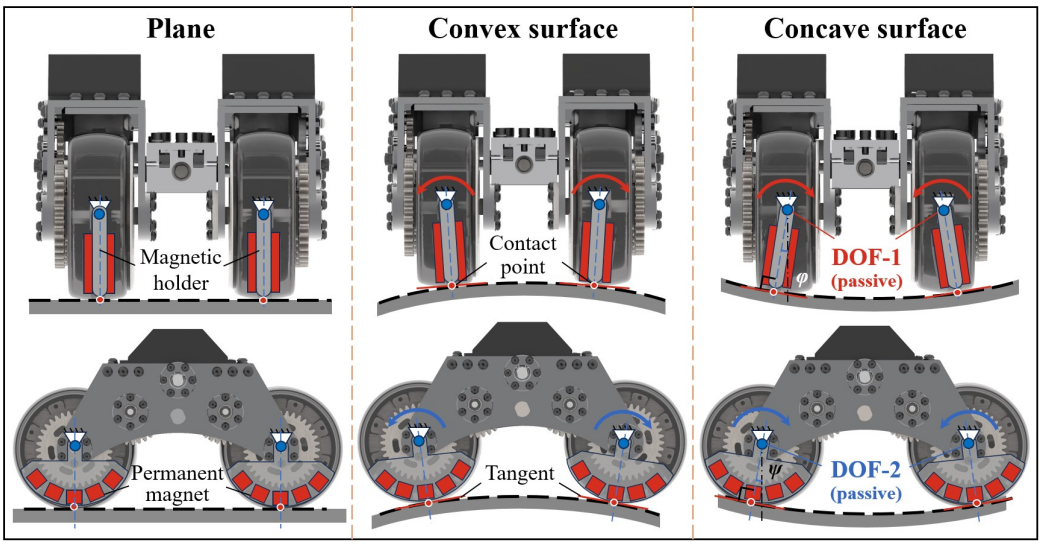


Figure 3. Motion posture of magnet holder.

3. Static Analysis of the Robot

3.1. Analysis of Failure Conditions

Magnetic adhesion plays a key role in ensuring the stable locomotion of the robot on inclined surfaces. Insufficient magnetic adhesion will cause the robot to overturn longitudinally and transversely, while insufficient friction will result in slipping. Figure 4a shows the static analysis of forces acting on the robot during longitudinal motion on the wall, where point A is the longitudinal overturning point of the robot. In the analysis, the following simplifying assumptions are made: the magnetic adhesion force is approximated as acting along the normal direction of the contact surface, and its tangential component is neglected. In addition, the robot is analyzed under quasi-static equilibrium, ignoring inertial and dynamic effects. These assumptions are valid for low-speed and quasi-static operating conditions. To prevent longitudinal overturning, the moment generated by the adhesion about the overturning point must overcome the gravitational moment about the same point, which can be expressed as

$$L(F_{m1} + F_{m3}) \geq k\left[(G + F_g)H\cos\alpha + \frac{(G + F_g)L\sin\alpha}{2}\right] \quad (1)$$

where α is the wall tilt angle, k is the safety coefficient, and L is the longitudinal wheel spacing. H is the height from the robot's center of mass to the surface in contact. $F_{mi}(i = 1,2,3,4)$ is the adhesive force generated by a single magnetic spherical wheel. G is the gravity of the robot. F_g is the gravity of the payload.

Under this condition, the necessary magnetic adhesion force for each magnetic spherical wheel is given by

$$F_{mi} \geq k\left[\frac{(G+F_g)H\cos\alpha}{2L} + \frac{(G+F_g)\sin\alpha}{4}\right] \tag{2}$$

Slip occurs when the portion of the robot's weight along the z-axis exceeds the friction generated by magnetic adhesion. This threshold condition is formulated as

$$\mu F_{N1} + \mu F_{N2} + \mu F_{N3} + \mu F_{N4} = (G+F_g)\cos\alpha \tag{3}$$

where μ is the coefficient of friction, F_N is the normal force.

Under the condition that the robot does not experience slipping, the required adhesion force for a single magnetic spherical wheel is given by

$$F_{mi} \geq k\left(\frac{(G+F_g)\cos\alpha}{4\mu} + \frac{(G+F_g)\sin\alpha}{4}\right) \tag{4}$$

Figure 4b illustrates the forces exerted on the robot during transversely movement along the wall, with point B being the transverse overturning point of the robot. To prevent transverse overturning, the equation can be expressed as

$$W(F_{m1} + F_{m3}) \geq k\left[(G+F_g)H\cos\alpha + \frac{(G+F_g)W\sin\alpha}{2}\right] \tag{5}$$

where W is the transverse wheel spacing.

Under the condition that transverse overturning of the robot is prevented, the required adhesion force for a single magnetic spherical wheel is given by

$$F_{mi} \geq k\left[\frac{(G+F_g)H\cos\alpha}{2W} + \frac{(G+F_g)\sin\alpha}{4}\right] \tag{6}$$

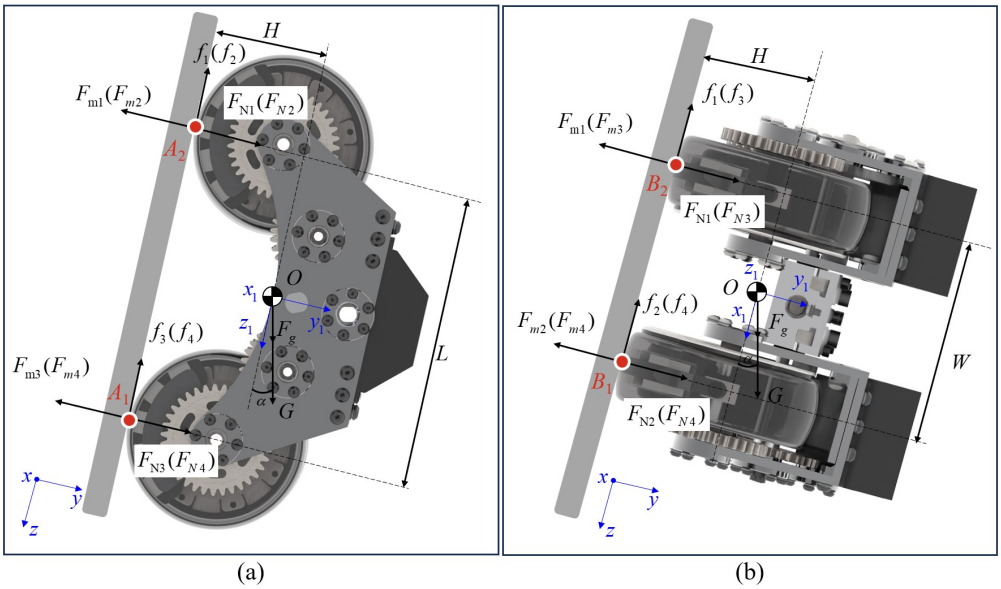


Figure 4. Statics analysis diagram: (**a**) Longitudinal stability. (**b**) Transverse stability.

3.2. Comparative Analysis of Failure Conditions

Table 2 provides the dimensional parameters of the robot. By applying Equations (2), (4) and (6) with the corresponding values, the relationship between the minimum adhesion force of a single magnetic spherical wheel and the tilt angle of the contact surface is determined, as shown in Figure 5. The adhesion force required to prevent slipping consistently exceeds that needed to prevent overturn. With an increase in the tilt angle, the minimum adhesion force of a single spherical wheel initially rises and then decreases. At a tilt angle of $\alpha = 22°$, the required minimum adhesion force reaches its maximum value of 75.73 N.

Table 2. Robot dimensional parameters.

G/N	F_g/N	L/mm	H/mm	W/mm	k	μ
60	15	200	76.5	116.6	1.5	0.4

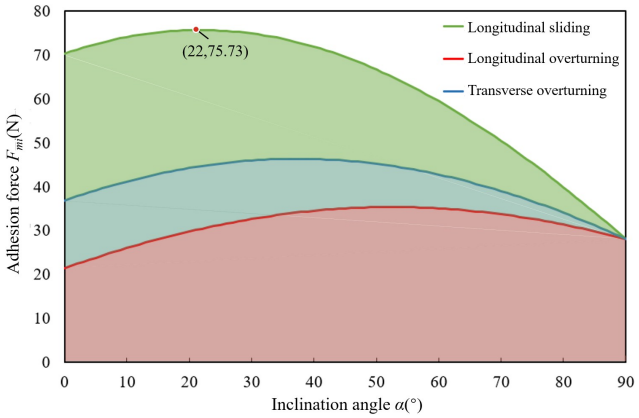


Figure 5. The adhesive force F_{mi} varies with the wall tilt angle α.

4. Magnetic Simulation Analysis of the Magnetic Spherical Wheel

4.1. Biaxial Floating Magnetic Circuit Design

The magnets are fixed to an aluminum magnet holder, which serves to house the permanent magnets. Both the magnet holder and the spherical shell are made of aluminum, ensuring sufficient structural strength while minimizing interference with the magnetic field. To improve magnet utilization and maintain alignment with the spherical shell, the magnet holder is designed with an arc-shaped profile. The permanent magnets are made of NdFeB-N52 material.

An efficient magnetic circuit design can effectively reduce the overall weight of the robot. We selected three different magnetic circuit designs for comparative analysis, as shown in Figure 6. The first is the Halbach magnetic circuit, which achieves unilateral magnetic field enhancement and field weakening on the opposite side. In the second design, the magnets have the same magnetization direction. In the third design, adjacent magnets possess opposite magnetization directions.

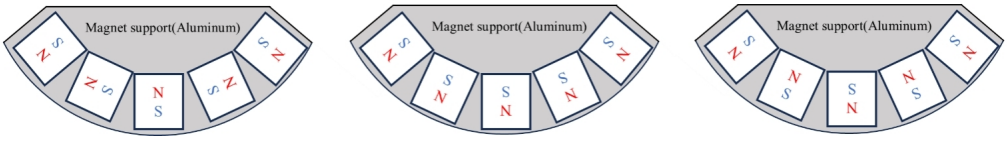


Figure 6. Different magnetic circuit structures of the magnet holders.

Simulation analysis was carried out on the three magnetic circuits separately using ANSYS 24 R1 Maxwell software, with the corresponding results presented in Figure 7.

From these results, it is evident that, assuming all other parameters (e.g., magnet size and material) remain constant except for the magnetization direction, different magnetic circuit designs produce different magnetic adhesion forces, which decrease with the increase in air gap. Among the designs, the Halbach configuration achieves the maximum adhesion force and the most efficient magnetic circuit performance at the same air-gap distance, and is thus selected for implementation.

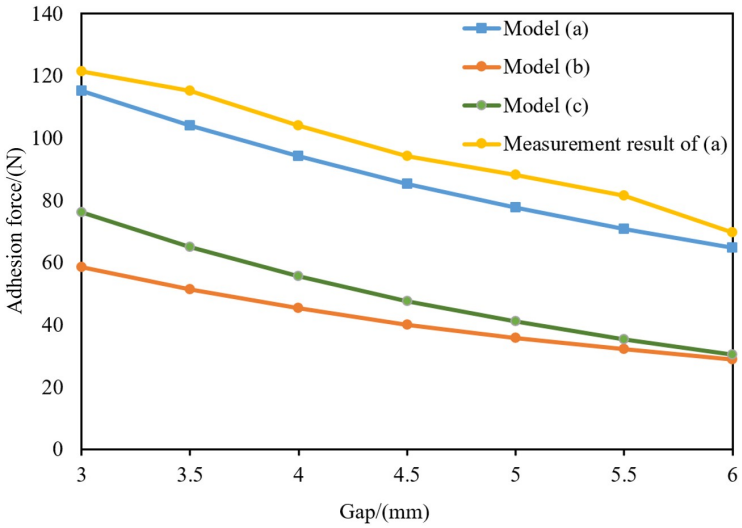


Figure 7. The relationship between the gap and the adhesion force.

4.2. Adhesive Force Analysis in Magnet Arrays

To verify that a single permanent magnetic spherical wheel can provide sufficient adhesive force, as required in Section 2, a magnetic simulation analysis of the entire permanent magnetic spherical wheel was conducted. The structural configuration of the permanent magnetic spherical wheel is shown in Figure 8, and its detailed dimensional specifications are listed in Table 3.

Table 3. Design parameters of the magnetic spherical wheel.

a/mm	*b*/mm	*c*/mm	*d*/mm	*T*/mm	*t*/mm	*r*/mm	*θ*/°	*g*/mm
15	20	20	1.5	2	20	57	25	1

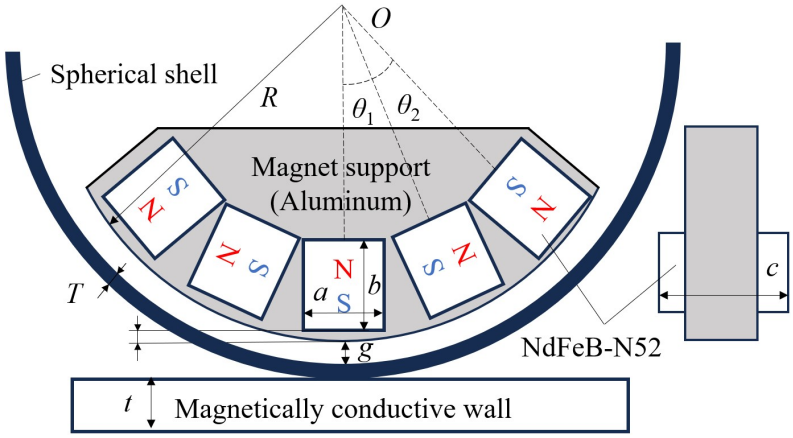


Figure 8. Structural diagram of the magnetic spherical wheel.

Figure 9 illustrates the magnetic field distribution of the spherical magnetic wheel. The magnetic field intensity is mainly concentrated on the side adjacent to the ferromagnetic

wall, while it decreases significantly on the opposite side, exhibiting a clear single-sided concentration characteristic. In the contact region, the magnetic flux lines are densely distributed and predominantly oriented normal to the surface, whereas the tangential components near the edges are relatively small and symmetrically distributed, thus largely canceling each other. This indicates that the magnetic adhesion force is mainly aligned with the surface normal, thereby supporting the validity of the normal force assumption adopted in Section 2. Meanwhile, the simulated magnetic adhesion force is 98.547 N, which satisfies the minimum magnetic adhesion requirement.

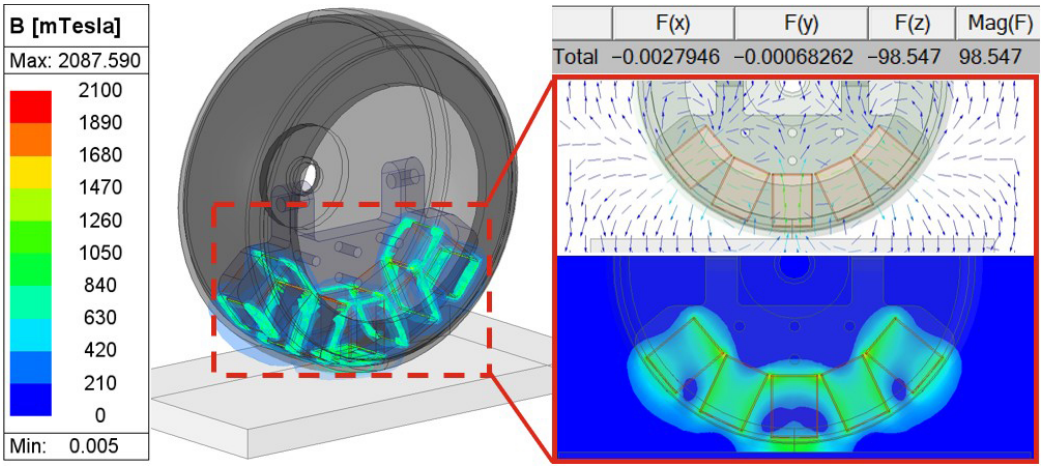


Figure 9. Magnetic simulation results.

As the robot traverses surfaces of varying curvature, the magnet holder within each spherical wheel swings in a direction orthogonal to the wheel's rotation (Figure 10a). The magnetic force generated by the spherical wheel reaches its peak when the magnet holder is aligned perpendicular to the local surface. Owing to the internal structure of the magnetic spherical wheel, the maximum swing of the magnet holder is φ_1 on concave surfaces and φ_2 on convex surfaces. Even when the holder is not perfectly normal to the surface, it can still generate sufficient magnetic force to satisfy the robot's static stability requirements. The maximum swing angles to meet these requirements are φ_3 for concave surfaces and φ_4 for convex surfaces.

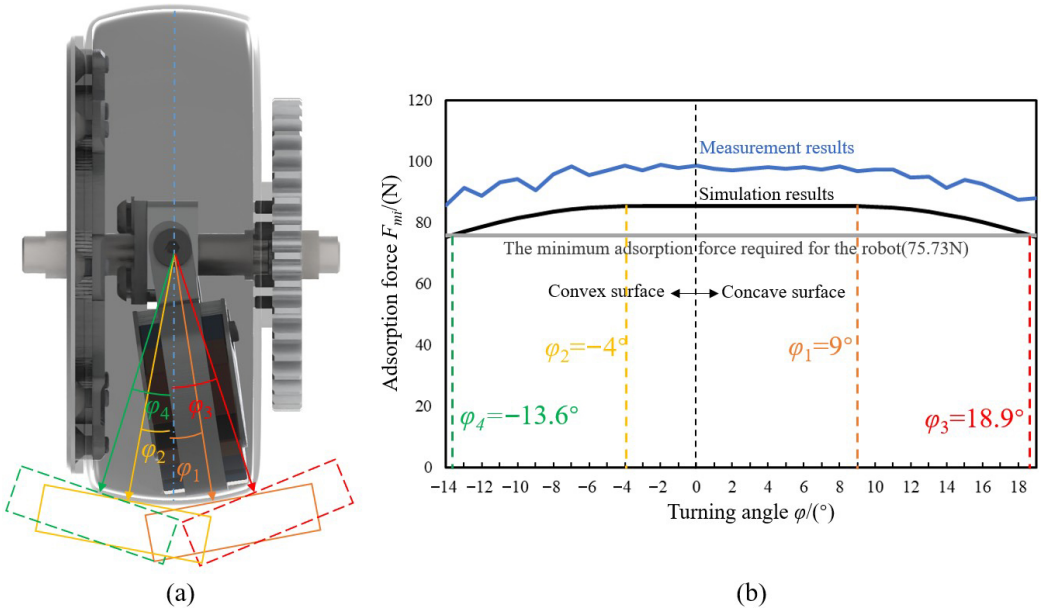


Figure 10. Swinging of the magnet holder: (**a**) Structural diagram. (**b**) Variation curve.

Figure 10b provides the simulation values and measured values, with an error of 2%. Under the same volume, the traditional permanent magnet wheel weighs 3562 g, while the proposed spherical wheel weighs 755 g, achieving a 79% weight reduction for magnetic wheels of identical size. Meanwhile, under the same magnetic adhesive force, the traditional permanent magnet wheel has a diameter of 60 mm, whereas the proposed spherical wheel measures 120 mm, doubling the size (a 100% increase) while maintaining equivalent adhesion performance, thereby offering enhanced obstacle-crossing performance.

5. Morphological Compliance for Curved-Surface Mobility

5.1. Biaxial Floating Magnet Adaptability to Curved Surfaces

Within each spherical wheel of the climbing robot, the magnet holder undergoes passive swinging in response to the wall's curvature due to magnetic forces. By examining the swing angle of this holder, the robot's capability to adapt to the curvature during longitudinal motion can be evaluated. The posture of the robot during axial movement on a curved wall is shown in Figure 11a. The swing angle φ of the magnet bracket can be expressed as follows for convex and concave surfaces, respectively:

$$\varphi = \begin{cases} \arcsin\left(\dfrac{W/2}{R + D/2}\right), & \text{convex surface} \\ \arcsin\left(\dfrac{W/2}{R - D/2}\right), & \text{concave surface} \end{cases} \tag{7}$$

where φ denotes the magnet holder's swing angle, R denotes the curvature radius, and D denotes the diameter of spherical shell.

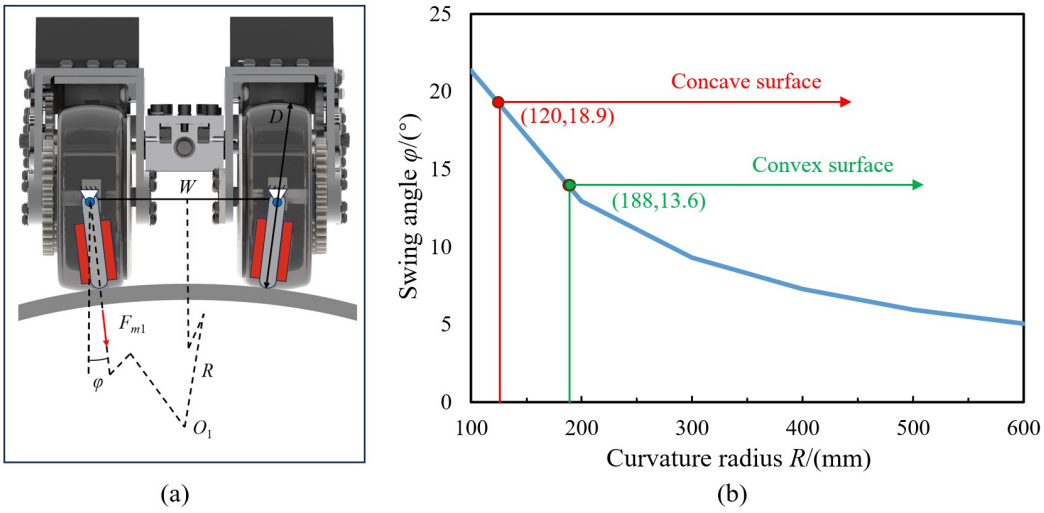


Figure 11. Analysis of the curvature adaptability of the magnet holder: (**a**) Schematic of magnetic holder orientation variation. (**b**) Relationship between swing angle and curvature radius.

Figure 11b presents the variation in the swing angle with respect to the curvature radius. The results indicate that the swing angle gradually decreases as the curvature radius becomes larger. Based on the allowable maximum swing angle, the smallest curvature radius that the robot can accommodate is 120 mm for concave surfaces and 188 mm for convex surfaces.

5.2. Curvature-Adaptive Compliance of Mechanical Cantilevers

To prevent excessive mechanical cantilever rotation, it is necessary to determine the impact of surface curvature and robot turning angle θ on the pitch angle β. The pitch angle is defined as the angle formed by the mechanical cantilever relative to the local

horizontal direction of the surface. For convenience in the mathematical derivation while maintaining general applicability, two assumptions are introduced. First, the pipe robot is modeled as a rigid vehicle equipped with non-deformable wheels. Second, due to the square frame structure of the robot, the distance from the robot's center of mass to the pipe center remains constant during turning. Figure 12 illustrates the configuration of the robot turning diagonally along a curved surface. From this layout, the following relationship can be established:

$$\begin{cases} L_2 = \dfrac{L_1}{\tan\theta}, \\ \dfrac{x_0 \sin^2\theta}{R^2} + \dfrac{y_0}{R^2} = 1, \\ k_{MP} = \dfrac{y_0 - L_3}{x_0 + L_2}, \\ k_{EF} \cdot k_{MP} = -1 \end{cases} \tag{8}$$

where L_1 is the length between the center of mass of the robot and the mechanical cantilever, L_2 is the length from the center of the cantilever to the intersection between the cantilever and the central generatrix of the wall, L_3 is the length from the center of mass of the robot to the center of the curved surface, $P(x_0, y_0)$ is in the ellipse that coincides with EF, and N_1N_2 is parallel to EF. k_{EF} and k_{MP} are the slopes of EF and MP, respectively. MP is perpendicular to EF.

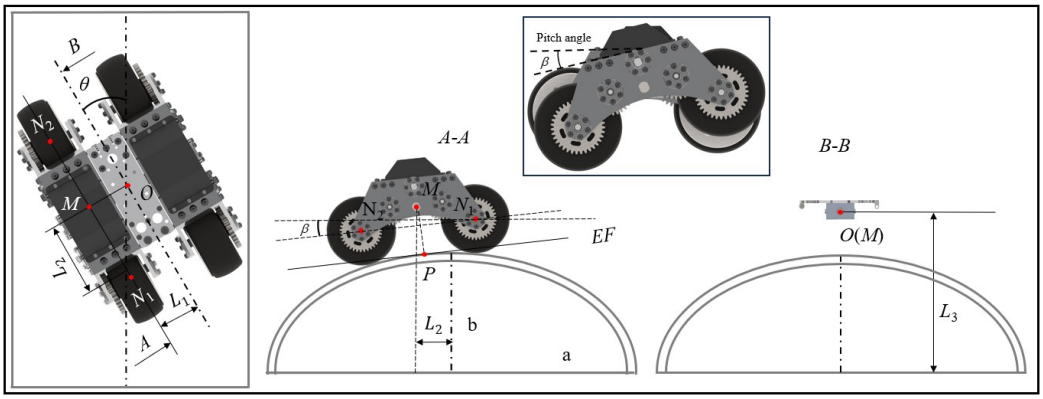


Figure 12. Mechanical cantilever posture change on convex surface.

According to Equation (8), the relationship between β , θ and R is expressed by

$$\begin{cases} k_{EF} = -\dfrac{(\sin\theta)^2 x_0}{y_0} \\ \beta = \arctan(k_{EF}) \end{cases} \tag{9}$$

By numerically evaluating Equations (8) and (9), the correlation between the steering angle θ and the pitch angle β for different curvature radii can be obtained, and the results are presented in Figure 13. When the robot operates on either concave or convex surfaces, excessive rotation of the mechanical cantilever must be prevented; therefore, the maximum allowable pitch angle is limited to 10°. Under this constraint, when the robot maintains its maximum adhesion force, it is capable of operating on surfaces with a curvature radius not smaller than 136 mm.

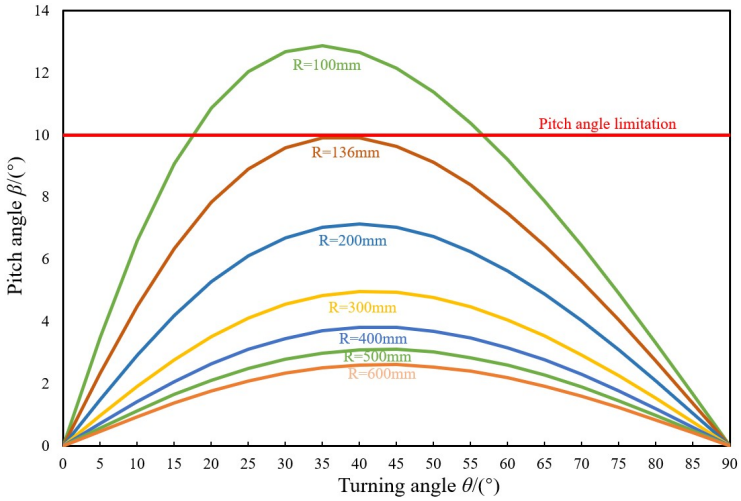


Figure 13. Variation curve for the pitch angle.

5.3. Curvature-Adaptive Compliance of Cantilever-Integrated Sensing

To ensure that the robot can conduct inspection tasks both efficiently and reliably, an array-based probe configuration is employed. A total of seven electromagnetic ultrasonic probes are mounted beneath the robot and organized into four groups, as illustrated in Figure 14. The spacing between each probe center and the contact surface has a direct influence on the detection accuracy. Therefore, when the robot travels across a curved surface, it is necessary to analyze the variation in the gap between the probe centers of the four groups and the surface at different positions.

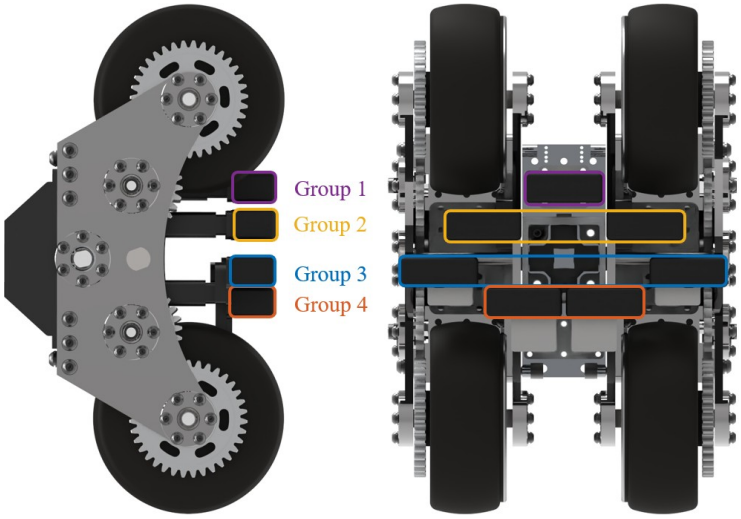


Figure 14. Probe arrangement on the robot.

Figure 15a presents the geometric configuration of the probes when the robot travels circumferentially along the outer surface of the pipeline. The contact point $p(x_p, y_p)$ between the probe and the surface, the probe center point $s(x_s, y_s)$, and the intersection point $q(x_q, y_q)$ of the probe's centerline with the circle O are depicted. Points p and q lie on the circle O, with R representing the radius of the circle. Therefore, the equation can be expressed as

$$\begin{cases} x_p^2 + y_p^2 = R^2 \\ x_q^2 + y_q^2 = R^2 \end{cases} \tag{10}$$

The probe gap δ between the probe center and the surface is the distance between points s and q, which can be expressed as:

$$\delta = \begin{cases} |y_s - y_q|, & w \neq 0, \\ 0, & w = 0 \end{cases} \tag{11}$$

Considering the spatial relationship between the probe and the center of the robot, together with the width of the probe, the coordinate of the contact point in the x-direction can be written as $x_p = w - \frac{b}{2}$. Since both points s and p lie on the bottom surface of the probe, $y_s = y_p$. By combining Equations (10) and (11), $\delta = f(R, w, b)$ can be expressed as

$$\delta = \begin{cases} \left| \sqrt{R^2 - (w - b/2)^2} - \sqrt{R^2 - w^2} \right|, & w \neq 0, \\ 0, & w = 0 \end{cases} \tag{12}$$

The state of the probe when the robot moves axially along the outer side of the pipeline is similar to the state during axial motion. However, due to the changes in the contact point of the probe with the pipeline and the relative position of the probe to the robot's center, the probe gap $\delta = f(R, w, b)$ can be expressed as

$$\delta = \begin{cases} \left| \sqrt{R^2 - (l - a/2)^2} - \sqrt{R^2 - l^2} \right|, & l \neq 0, \\ 0, & l = 0 \end{cases} \tag{13}$$

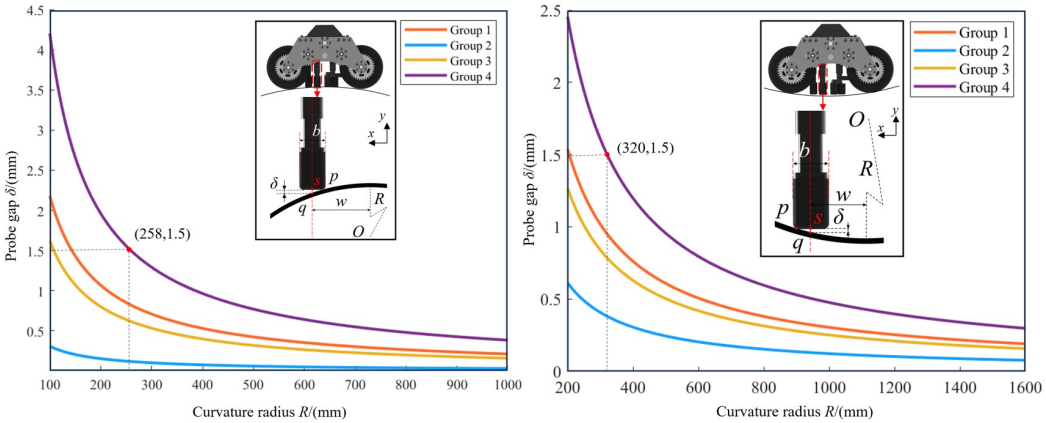


Figure 15. Analysis of probe gap in robot circumferential motion: (**a**) Convex surface. (**b**) Concave surface.

Figure 15a,b illustrate the variation in the probe gap of the four different groups of probes with respect to the curvature radius during the robot's circumferential and axial movements along the outer side of the pipeline. As the curvature radius changes from 100 mm to 1000 mm, affected by the lift effect, the recommended maximum probe gap for the electromagnetic ultrasonic probe is $\delta \leq 1.5$ mm. Regardless of whether the robot is moving circumferentially or axially, the probe gap decreases as the curvature radius increases. During circumferential motion, the probe in Group 4 is located at the largest distance from the robot center. To meet the recommended probe gap, the smallest curvature radius at which the robot can operate is 258 mm. During axial motion, the probe in Group 2 has the greatest offset from the robot center, and the robot can operate at a minimum curvature radius of 990 mm. Therefore, when the robot with probes operates on a convex surface, the minimum curvature radius that ensures proper probe functionality is 990 mm.

Figure 16a presents the changes in probe clearance for the four probe groups as the robot moves circumferentially along the inner surface of the pipeline, and Figure 16b shows the corresponding schematic layout. The relationship for the probe gap δ can be expressed as

$$\delta = \begin{cases} \left| \sqrt{R^2 - (w + b/2)^2} - \sqrt{R^2 - w^2} \right|, & \text{Circumferential motion,} \\ \left| \sqrt{R^2 - (l + a/2)^2} - \sqrt{R^2 - l^2} \right|, & \text{Axial motion} \end{cases} \tag{14}$$

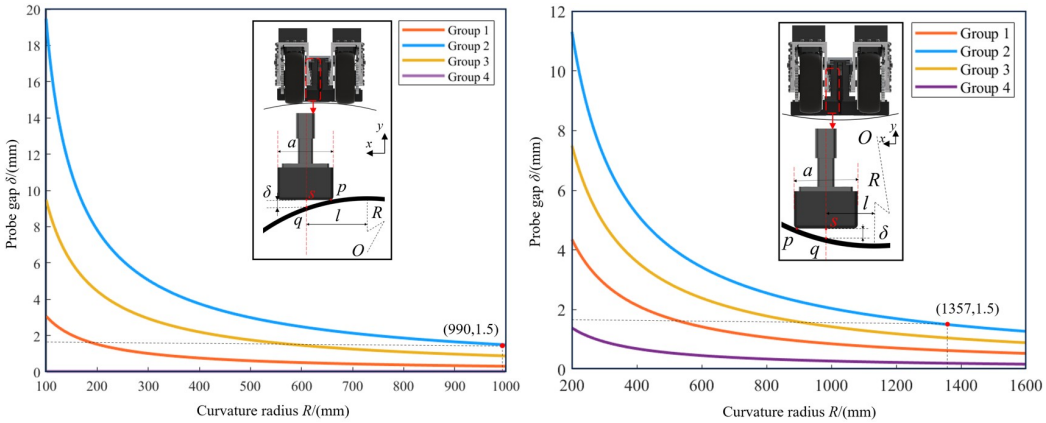


Figure 16. Analysis of probe gap in robot axial motion: (**a**) Convex surface. (**b**) Concave surface.

When the robot moves circumferentially along the inner side of the pipe, the probe in Group 4 is the furthest from the robot's center. To satisfy the recommended probe clearance, the robot requires a curvature radius no less than 320 mm. During axial motion, the probe in Group 2 is the farthest from the robot's center, and the robot can operate at a minimum curvature radius of 1357 mm. Therefore, when the robot with probes operates on a concave surface, the minimum curvature radius that ensures proper probe functionality is 1357 mm.

6. Experimental Validation in Laboratory and Field Environments

Figure 17 presents the C3bot prototype. For the actuating system, the DYNAMIXEL XM540-W270R from ROBOTIS Co. Ltd. (Seoul, Republic of Korea) is used, offering a rated torque of 6 Nm (max 10.2 Nm). The total mass of the robot amounts to 7.5 kg, including inspection probe, lighting unit, and top housing, with a payload capacity of 16.67 kg. The robot housing materials are selected to ensure structural strength while reducing the overall weight. Following static evaluation and simulations of the magnetic spherical wheels, the adhesion mode of Model(a) was selected. The battery inside the control box supplies power to the robot body. Commands from the handle are transmitted to the wireless receiving module in the control box to operate the robot. The robot's travel velocity can be adjusted between 0 and 6 m/min to meet different speed requirements.

In addition, systematic experimental validations were conducted to evaluate the robot's performance, including adhesion and friction measurements, climbing tests under different curvature conditions, payload and obstacle-crossing assessments, and inspection tasks in a real turbine blade scenario. These experiments provide a comprehensive evaluation of the robot in terms of fundamental mechanical performance, adaptability to complex environments, and feasibility in practical industrial applications, with consistent and stable results observed across repeated trials. The prototype operates at a rated current of approximately 15 A and is powered by an external 20,000 mAh battery pack, enabling at least 8 h of continuous operation in field environments without external power sources.

The power unit integrates an STM32-based control board and an automatic cable reel mechanism to regulate cable length during operation.

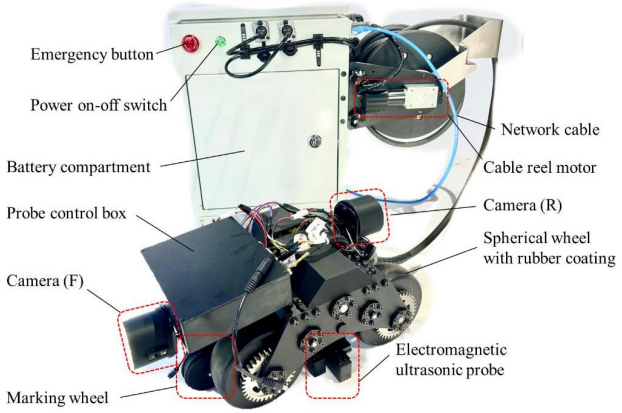


Figure 17. Prototype of wall-climbing robot.

6.1. Permanent Magnetic Adhesive Force Test

As shown in Figure 18a, the variation in the adhesion force was measured by changing the tilt angle of the magnet assembly. The experimental data, shown in Figure 10b, represents the average of three measurements. The decay trend is generally consistent with the simulation outcomes, falling within a 10% margin of error.



(a) (b) (c)

Figure 18. Magnetic spherical wheel performance test: (**a**) Swinging of the magnet holder test. (**b**) Friction test. (**c**) Acrylic plates of different thickness.

Figure 18b illustrates the composition of the magnet assembly, including permanent magnets (NdFeB-N52), a shaft, a magnet holder, dual bearings, a hollow wheel hub, and a rubber coating. Each permanent magnet has dimensions of 20 mm × 20 mm × 15 mm, consistent with the model design shown in Figure 8. To facilitate the measurement of the friction coefficient of the spherical wheel, only a single permanent magnet was installed in each wheel during the test. The spherical wheel was placed on the top surface of a pipe, and a vertical pulling force was applied until detachment occurred. The measured force was 1.45 kg, while the weight of the wheel was 0.23 kg, resulting in an effective magnetic adhesion force of approximately 1.22 kg. To eliminate the influence of gravity during the lateral friction test, the wheel was attached to the side surface of the metal pipe, where the normal force was solely provided by magnetic adhesion. Under this condition, the maximum static friction forces of the wheels with and without the rubber coating were 0.48 kg and 0.18 kg, corresponding to friction coefficients of 0.39 and 0.15, respectively. Compared with the uncoated wheel, the maximum static friction force increased by approximately 2.6 times.

As shown in Figure 18c, the test wall is constructed from Q235 steel with a thickness of $T = 5$ mm. Acrylic-plates of varying thicknesses are used to adjust the gap G within 1.5–4.5 mm. Figure 7 presents the adhesion force of the magnet assembly measured under the specified experimental conditions. The design achieves a weight reduction of 79% for magnet assembly of identical size; for magnet assembly with the same adhesive force, the size is increased by 100%, providing enhanced obstacle-crossing performance.

6.2. Mobility Performance Evaluation in Controlled Environments

6.2.1. Moving on the Vertical Wall

Figure 19 illustrates the robot performing a zigzag trajectory on a vertical plane ($R = \infty$). The robot traveled at an approximate velocity of 33 mm/s, and it took about 1 min to traverse the entire surface. The experimental results show that no failure phenomena, such as slipping or overturning, occurred during longitudinal motion, transverse motion, or turning. The robot maintained good contact with the surface throughout the motion and was able to effectively accomplish the intended climbing task, thereby verifying its adhesion capability.

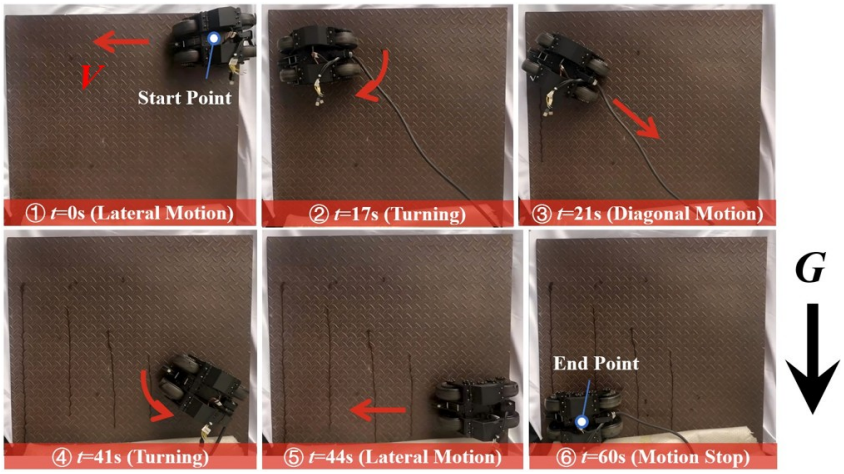


Figure 19. The wall-climbing robot performs a zigzag motion on the vertical wall.

6.2.2. Adaptive Surface Movement on the Concave and Convex Facades

The robot's adaptability was evaluated on metal pipes with varying curvature. Owing to the passive adaptive magnetic wheel mechanism, the driving modules maintain stable contact with the curved surface. This demonstrates the feasibility of the proposed mechanism design, as illustrated in Figures 20–22. To further investigate the robot's motion capability on spatial curved structures, additional tests involving rotational movement on cylindrical pipes were carried out. During these trials, the robot completed spiral trajectories along the pipe surfaces, covering both internal and external paths. Experiments were conducted on the exterior surfaces of pipes with curvature radii of 100 mm, 150 mm, and 350 mm, as well as on the interior surface of a pipe with a radius of 350 mm. These results demonstrate the robot's stable and flexible locomotion on variable-curvature surfaces. Table 4 summarizes the success rates of different locomotion modes under five repeated trials. The results indicate that the robot consistently maintains high motion success rates and stable performance on complex variable-curvature surfaces, demonstrating strong robustness and locomotion flexibility.

Figure 20a–c illustrate different motion processes of the robot on a 90° elbow pipe. According to the robot's working principle, when the robot contacts the outer surface of the pipe (convex surface), the contact point is located on the inner side of the spherical wheel, causing the magnet holder to swing inward and ensuring that all four wheels to remain

firmly attached to the contact surface.In addition, the pipe elbow contains two weld seams with heights ranging from 3 to 7 mm. The robot can stably traverse these obstacles from multiple directions and successfully pass through the entire elbow section. According to the repeated experimental results in Table 4, straight-line motion on a 150 mm pipe achieved a 100% success rate, indicating stable adhesion performance.In contrast, one detachment event occurred during spiral motion under the same condition. This is mainly attributed to the fact that the normal force of the pipe surface introduces a resistance component opposite to the motion direction, increasing the difficulty of maintaining stable adhesion. As shown in Figure 20c, the robot moves by spirally wrapping around the outer side of the pipe. During this process, both the magnet support and the cantilever swing angle can passively adjust to automatically adapt to the contact condition at any moment.

Figure 21 presents the robot executing spiral locomotion along a pipe with a radius of 100 mm. According to the theoretical analysis, the smallest curvature radius the robot is designed to accommodate is 120 mm, at which point the magnetic adhesion force satisfies a safety factor of 1.5. However, the results show that the robot is capable of adapting to surfaces with even smaller curvature radii. According to Table 4, the success rate of spiral motion on the 100 mm pipe is 80%, with one detachment and one slippage observed. This is mainly due to increased resistance from normal force under reduced curvature and a smaller contact area, which makes the robot more prone to insufficient contact or partial suspension. In addition, the automatic cable retraction system allows the robot to perform spiral motion along the pipeline more flexibly.

Table 4. Success rate of repeated experiments under different locomotion modes.

Locomotion Mode	Success Rate (10 trials)
Top generatrix climbing (R = 150 mm)	100%
Side generatrix climbing (R = 150 mm)	100%
Spiral motion (outer surface, R = 100 mm)	90%
Spiral motion (outer surface, R = 100 mm)	80%
Spiral motion (outer surface, R = 350 mm)	100%
Spiral motion (inner surface, R = 350 mm)	90%

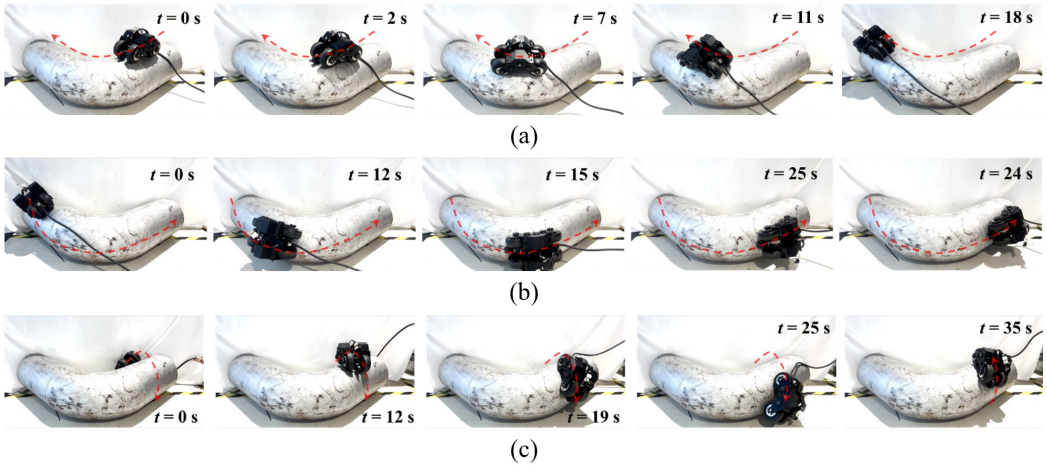


Figure 20. Robot locomotion on a pipe with an outer radius of 150 mm and wall thickness of 5 mm: (**a**) The robot travels along the top generatrix. (**b**) The robot traverses the side generatrix. (**c**) The robot follows a spiral trajectory around the pipe's exterior.

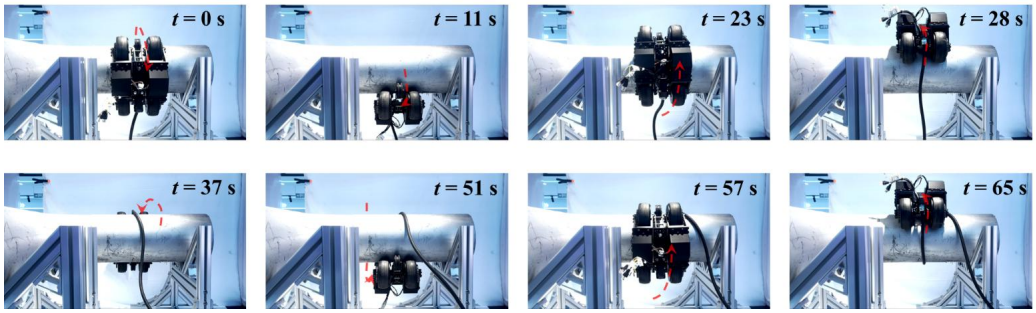


Figure 21. Circular locomotion of the robot along the exterior of a pipe with an outer radius of 100 mm and a wall thickness of 5 mm.

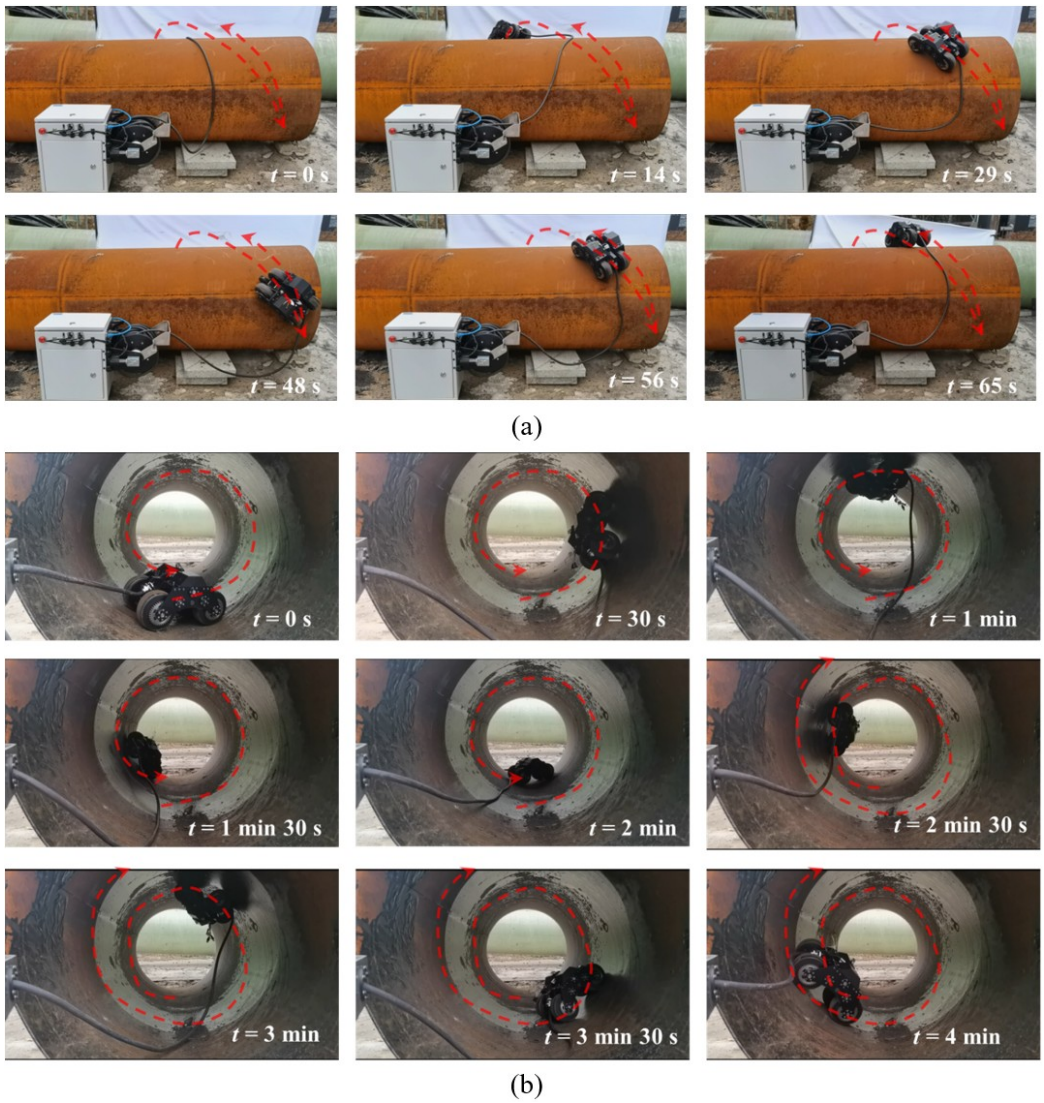


Figure 22. Locomotion of the robot along a 350 mm radius pipe: (**a**) Helical movement around the pipe's outer wall. (**b**) Helical movement along the pipe's inner wall.

Figure 22 shows the robot moving along both the inner and outer surfaces of a large-diameter pipeline with a radius of 350 mm. The robot can operate stably on metal surfaces covered with rust and can also traverse weld seams with heights ranging from 2 to 5 mm. According to Table 4, the success rate of spiral motion on the outer surface of the 350 mm pipe is 100%, while one slippage occurs during inner-surface locomotion, mainly at the bottom of the pipe. This is attributed to dense debris accumulated at the bottom, which significantly weakens magnetic adhesion and leads to insufficient friction. In such complex

and harsh environments, the floating magnetic spherical wheel structure does not attract metal debris across the entire wheel surface as a permanent magnetic wheel would. Instead, iron particles are mainly attracted only where the wheel contacts the surface, thereby keeping most of the ball-wheel surface clean. These results highlight the robot's strong capability to function in complex industrial environments.

6.2.3. Obstacle-Crossing Capability and Payload Capacity Tests

As shown in Figure 23a, a load-bearing locomotion experiment was conducted on a ferromagnetic wall with a thickness of 2 mm. A tension meter was fixed to the ground and connected to the robot, while the two groups of drive motors on the robot were activated simultaneously. During the experiment, the maximum recorded tension reached 166.3 N, which is approximately 2.2 times the weight of the robot. This result confirms that the robot has a strong load-bearing capability and is able to meet the operational demands of inspection tasks.

The safety rope is one of the key safety configurations for the wall-climbing robot during operation, significantly improving operational reliability and preventing potential accidents. Figure 23b presents the robot in adhesion to a 90° vertical wall. By pulling the safety rope connected to the tail, vertical displacement of the robot can be achieved, enabling upward and downward movement along the planar surface. This demonstrates that in the event of power loss or drive failure, the robot can be manually retrieved to a safe position by pulling the safety rope. Therefore, safe operation can still be ensured even under emergency conditions.

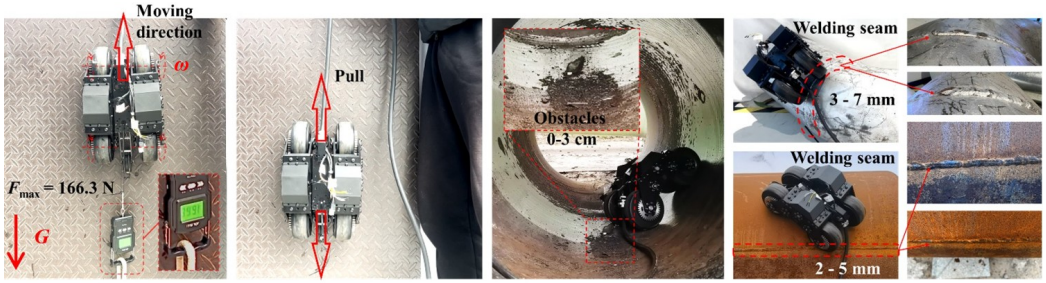


Figure 23. Basic Testing: (**a**) Vertical load test of the robot. (**b**) Safety rope test for the robot. (**c**) Robot navigation through obstacles inside pipelines. (**d**) Robot traversal over weld seams on the exterior of pipes with varying radius.

Figure 23c,d present the tests of the robot traversing weld seams on the outer surface of the pipe and dense debris obstacles inside the pipe. The robot successfully navigated along pipe surfaces with different curvatures and reliably overcome obstacles measuring 2–7 mm in height on both the inner and outer walls. These experiments confirm that the proposed climbing robot can effectively handle complex surface conditions and obstacles commonly encountered in industrial pipeline inspection and maintenance tasks.

6.3. Field Deployment in Hydropower Facilities

The robotic inspection site is located at a hydroelectric power station's turbine unit in the southwestern region, China. The hydropower station utilizes Francis turbines, with the robotic inspection focusing on the turbine runner. The runner, which is made of ZG04Cr13Ni4Mo cast stainless steel, has a radius of 8.9 m, a height of 3.59 m, and consists of 15 blades, as illustrated in Figure 24a. After a period of operation, the runner exhibits multiple defects, including rust, scratches, and cavitation damage, as shown in Figure 24b. Figure 24c presents the operational data transmitted by cameras and Magnetic Flux Leakage (MFL) probes. The acquired data is visualized as color-coded mapping on the

host computer interface. The robot utilizes front/rear cameras for positioning verification, while its probes measure surface defects with 0–1 mm depth resolution. Figure 24d,e demonstrate the robot operating on inverted and vertical surfaces, respectively. The robot traverses the surface of runner blades in a zigzag pattern at a speed of approximately 6.5 m/min, achieving full coverage inspection of the turbine runner. Compared to the traditional manual inspection method involving scaffold erection beneath the runner, robotic inspection technology demonstrates significant advantages in confined spaces like turbine runners: higher efficiency, superior precision, and enhanced safety.

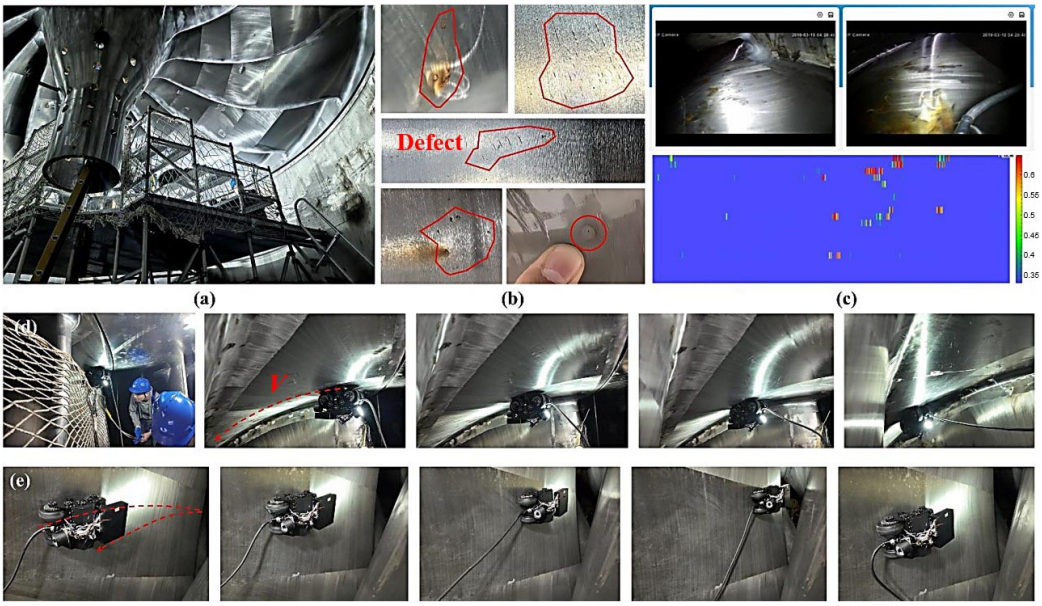


Figure 24. On-site Testing: (**a**) Turbine runner. (**b**) Defect in runner blades. (**c**) Inspection results of electromagnetic ultrasonic probes and cameras (**d**) Robotic inverted surface inspection. (**e**) Robotic vertical surface inspection.

Table 5. Performance metrics of the C3bot.

Projects	Experimental Parameters
Weight	7.5 kg
Load capacity	16.6 kg (vertical plane (Q235) 5 mm)
Size	315 × 210 × 176 mm
Moving speed	0–8 m/min
Working environment	Without ultrasonic probes: R = 120 mm (Concave), R = 188 mm (Convex), With ultrasonic probes: R = 990 mm (Concave), R = 1357 mm (Convex).
Cross-barrier capability	8 mm without ultrasonic probes and 5 mm with ultrasonic probes
Parameters of cameras	2 cameras, Pixel: 1920 × 1080, Fill light
Maximum working distance	10 m
Auxiliary emergency measure	Safety-rope traction to prevent falling

In conclusion, during repeated trials, the robot showed no obvious failure such as detachment or slipping and was able to flexibly and stably perform various crawling motions on multiple three-dimensional curved surfaces. This demonstrates that the previously proposed structural design, as well as the theoretical analysis and simulation models, are reasonable and effective. The detailed motion testing process of the robot can be found in

Video S1: Climbing Robot Experiment. A summary of the robot's key functional parameters is provided in Table 5.

7. Conclusions

A novel wall-climbing robot intended for use in inspection tasks on three-dimensional surfaces with varying curvature is presented in this study. By integrating spherical wheels, a two-degree-of-freedom magnet holder, and a differential center, continuous and reliable adhesion between the robot and the working surface can be maintained. This configuration enables adaptive motion on curved surfaces without requiring complex control, while still maintaining a significant payload capacity.

The robot's failure modes under different motion states were analyzed through theoretical modeling and numerical simulations, revealing a minimum single-wheel magnetic adhesion force of 75.73 N (safety factor: 1.5) for stable operation. Comparative studies of magnetic circuits confirmed the Halbach array-based permanent magnet system as superior, optimized via parametric simulations for magnetic field distribution and adhesion performance. Key adhesion factors, including the spherical wheel's turning angle and contact surface geometry, were systematically examined. Mechanical limits—maximum cantilever pitch angle, minimum probe gap, and minimum adaptable curvature radius ($R_{\min}$)—were also determined, ensuring reliable operation on concave and convex surfaces..

Experimental validation demonstrated the robot's ability to passively conform to variable curvatures using its cantilever–spherical wheel system, achieving stable and agile locomotion even on tightly curved surfaces (e.g., $R = 100$ mm). The design's load-bearing capacity (166.3 N) and energy-efficient passive adaptation distinguish it from existing solutions, which often rely on complex actuators or sensors. These advancements highlight its potential for use in industrial maintenance applications where lightweight, adaptability, and reliability are critical. Future work will focus on improving the robot's capability for continuous transitions between heterogeneous surfaces in more complex irregular steel structures, as well as integrating onboard high-performance controllers, such as industrial PCs, to enable autonomous path planning and further expand its application scope.

Supplementary Materials: The following supporting information can be downloaded at https://www.mdpi.com/article/10.3390/machines14050492/s1. Video S1: Climbing Robot Experiment.

Author Contributions: Conceptualization, M.W. and J.Y.; Methodology, M.W. and Y.X.; Software, M.W. and Y.X.; Validation, M.W., Y.X. and Z.G.; Formal analysis, M.W. and Z.G.; Investigation, M.W., Y.X. and Z.H.; Resources, M.W., J.Y., S.B. and Z.H.; Data curation, Z.G.; Writing—original draft, M.W., Y.X. and Z.G.; Writing—review & editing, M.W., Z.G., J.Y., S.B. and Z.H.; Visualization, Z.G.; Supervision, J.Y., S.B. and Z.H.; Project administration, M.W., J.Y., S.B. and Z.H. All authors have read and agreed to the published version of the manuscript.

Funding: This research received no external funding.

Data Availability Statement: Data are contained within the article.

Acknowledgments: This article is a revised and expanded version of a paper entitled "Design and Validation of a Climbing Robot via Passive Wheel Compliance", which was presented at the 2025 IEEE International Conference on Cyborg and Bionic Systems (CBS), Beijing, China, 24–26 October 2025. Compared with the conference version [30], this work provides an expanded description of the robot design, additional analysis of the adhesion mechanism and curved-surface kinematics, and more comprehensive experimental validation.

Conflicts of Interest: The authors declare no conflicts of interest.

References

1. Wang, M.; Yuan, J.; Bao, S.; Du, L.; Ma, S. Robots for pipeline inspection tasks—A survey of design philosophy and implementation technologies. In Proceedings of the 2021 5th Asian Conference on Artificial Intelligence Technology (ACAIT), Haikou, China, 29–31 October 2021; pp. 427–432. [CrossRef]
2. Wang, M.; Bao, S.; Yuan, J.; Ma, S.; Guo, S.; Wan, W. Design and analysis of a robotic out-pipe grinding system with friction actuating. In Proceedings of the IEEE/RSJ International Conference on Intelligent Robots and Systems (IROS), Prague, Czech Republic, 27 September–1 October 2021; pp. 2467–2472. [CrossRef]
3. Liu, J.H.; Padrigalan, K. Design and development of a climbing robot for wind turbine maintenance. *Appl. Sci.* **2021**, *11*, 2328. [CrossRef]
4. Franko, J.; Du, S.; Kallweit, S.; Duelberg, E.; Engemann, H. Design of a multi-robot system for wind turbine maintenance. *Energies* **2020**, *13*, 2552. [CrossRef]
5. Han, L.; Wang, L.; Zhou, J.; Wang, Y. The development status of ship wall-climbing robot. In Proceedings of the 2021 4th International Conference on Electron Device and Mechanical Engineering (ICEDME), Guangzhou, China, 19–21 March 2021; pp. 231–237. [CrossRef]
6. Huang, H.; Li, D.; Xue, Z.; Chen, X.; Liu, S.; Leng, J.; Wei, Y. Design and performance analysis of a tracked wall-climbing robot for ship inspection in shipbuilding. *Ocean Eng.* **2017**, *131*, 224–230. [CrossRef]
7. Zhu, J.; Zhu, Y.; Zhang, P. Review of advancements in wall climbing robot techniques. *Frankl. Open* **2024**, *8*, 100148. [CrossRef]
8. Park, C.; Bae, J.; Ryu, S.; Lee, J.; Seo, T. R-track: Separable modular climbing robot design for wall-to-wall transition. *IEEE Robot. Autom. Lett.* **2020**, *6*, 1036–1042. [CrossRef]
9. Zhang, M.; Zhang, H.; Song, Q. Study on negative pressure adsorption characteristics of ship climbing robot. In Proceedings of the 2017 International Conference on Computer Technology, Electronics and Communication (ICCTEC), Karachi, Pakistan, 30–31 December 2017; pp. 1061–1067. [CrossRef]
10. Wu, S.; Wu, L.; Liu, T. Design of a sliding wall climbing robot with a novel negative adsorption device. In Proceedings of the 2011 8th International Conference on Ubiquitous Robots and Ambient Intelligence (URAI), Incheon, Republic of Korea, 23–26 November 2011; pp. 97–100. [CrossRef]
11. Kanada, A.; Giardina, F.; Howison, T.; Mashimo, T.; Iida, F. Reachability improvement of a climbing robot based on large deformations induced by tri-tube soft actuators. *Soft Robot.* **2019**, *6*, 483–494. [CrossRef]
12. Dong, X.; Zhang, R.; Tian, Y.; Ramos, M.A.; Hu, T.S.; Wang, Z.; Zhao, H.; Zhang, L.; Wan, Y.; Xia, Z.; et al. Functionally graded gecko setae and the biomimics with robust adhesion and durability. *ACS Appl. Polym. Mater.* **2020**, *2*, 2658–2666. [CrossRef]
13. Fang, Y.; Wang, S.; Bi, Q.; Cui, D.; Yan, C. Design and technical development of wall-climbing robots: A review. *J. Bionic Eng.* **2022**, *19*, 877–901. [CrossRef]
14. Lin, S.; Song, Y.; Wang, H.; Dai, J.; Lv, P.; Gao, W. Variable curvature adaptation and transformation flow of a passive-compliant magnetic wheeled wall-climbing robot. *Mech. Mach. Theory* **2023**, *189*, 105440. [CrossRef]
15. Tao, B.; Gong, Z.; Ding, H. Climbing robots for manufacturing. *Natl. Sci. Rev.* **2023**, *10*, nwad042. [CrossRef]
16. Jose, J.A.I.S.E.; Dinakaran, D.; Ramya, M.M.; Harris, D. A survey on magnetic wall-climbing robots for inspection. *Transst. J.* **2018**, *8*, 59–68. [CrossRef]
17. Tang, D.; Zhu, Z.; Yu, W.; Chen, X. A pneumatic soft pole-climbing robot with multi-gait function. *Mech. Sci. Eng.* **2026**, *48*, 218. [CrossRef]
18. Kang, S.; Yu, J.; Zhang, J.; Jin, Q. Development of multibody marine robots: A review. *IEEE Access* **2020**, *8*, 21178–21195. [CrossRef]
19. Hajeer, A.; Chen, L.; Hu, E. Review of classification for wall climbing robots for industrial inspection applications. In Proceedings of the 2020 IEEE 16th International Conference on Automation Science and Engineering (CASE), Hong Kong, China, 20–21 August 2020; pp. 1421–1426. [CrossRef]
20. Yang, P.; Sun, L.; Zhang, M. Design and analysis of a passive adaptive wall-climbing robot on variable curvature ship facades. *Appl. Ocean Res.* **2024**, *143*, 103879. [CrossRef]
21. Cui, S.; Pei, X.; Song, H.; Dai, P. Design and Motion Analysis of a Magnetic Climbing Robot Applied to Ship Shell Plate. *Machines* **2022**, *10*, 632. [CrossRef]
22. Eto, H.; Asada, H.H. Development of a wheeled wall-climbing robot with a shape-adaptive magnetic adhesion mechanism. In Proceedings of the 2020 IEEE International Conference on Robotics and Automation (ICRA), Paris, France, 31 May–31 August 2020. [CrossRef]
23. Hu, J.; Han, X.; Tao, Y.; Feng, S. A magnetic crawler wall-climbing robot with capacity of high payload on the convex surface. *Robot. Auton. Syst.* **2022**, *148*, 103907. [CrossRef]
24. Tavakoli, M.; Viegas, C.; Marques, L.; Pires, J.N.; De Almeida, A.T. OmniClimbers: Omni-directional magnetic wheeled climbing robots for inspection of ferromagnetic structures. *Robot. Auton. Syst.* **2013**, *61*, 997–1007. [CrossRef]
25. Jiang, Z.; Ma, Z.; Ju, Z.; Wang, D.; Xu, Y. Design and analysis of a wall-climbing robot for passive adaptive movement on variable-curvature metal facades. *J. Field Robot.* **2023**, *40*, 94–109. [CrossRef]

26. Wang, Y.; Zhang, X.; Zhang, M.; Sun, L.; Li, M. Self-compliant track-type wall-climbing robot for variable curvature facade. *IEEE Access* **2021**, *10*, 51951–51963. [CrossRef]
27. Khan, M.B.; Chuthong, T.; Do, C.D.; Thor, M.; Billeschou, P.; Larsen, J.C.; Manoonpong, P. iCrawl: An Inchworm-Inspired Crawling Robot *IEEE Access* **2020**, 8, 200655–200668. [CrossRef]
28. Bao, D.; Liang, X.; Ge, S.S.; Hou, B. A deep motion reliability scheme for robotic operations. *Mech. Mach. Theory* **2023**, *183*, 105280. [CrossRef]
29. Bao, D.; Liang, X.; Ge, S.S.; Hou, B. Adaptive neural trajectory tracking control for n-DOF robotic manipulators with state constraints. *IEEE Trans. Ind. Inform.* **2022**, *19*, 8039–8048. [CrossRef]
30. Xu, K.; Hu, M.; Deng, Z.; Wang, M.; Yuan, J.; Xu, Y. Design and Validation of a Climbing Robot via Passive Wheel Compliance. In Proceedings of the 2025 IEEE International Conference on Cyborg and Bionic Systems (CBS), Beijing, China, 17–19 October 2025; pp. 398–401. [CrossRef]

Disclaimer/Publisher's Note: The statements, opinions and data contained in all publications are solely those of the individual author(s) and contributor(s) and not of MDPI and/or the editor(s). MDPI and/or the editor(s) disclaim responsibility for any injury to people or property resulting from any ideas, methods, instructions or products referred to in the content.